Mesoporous iron sulfide nanoparticles anchored graphene sheet as an efficient and durable catalyst for oxygen reduction reaction

Jagadis Gautam [a], Duy Thanh Tran [a,**], Thangjam Ibomcha Singh [a], Nam Hoon Kim [a], Joong Hee Lee [a,b,*]

[a] Advanced Materials Institute for BIN Convergence Technology (BK21 Plus Global Program), Department of BIN Convergence Technology, Chonbuk National University, Jeonju, Jeonbuk, 54896, Republic of Korea
[b] Carbon Composite Research Center, Department of Polymer-Nano Science and Technology, Chonbuk National University, Jeonju, Jeonbuk, 54896, Republic of Korea

ARTICLE INFO

ABSTRACT

The fabrication of low-cost, highly efficient, and earth-abundant electrocatalysts for oxygen reduction reaction is critical to produce clean and sustainable fuel through an electrochemical process. Herein, a facile hydrothermal technique is used for the synthesis of iron sulfide/graphene hybrid for oxygen reduction reaction. Morphological analysis of the resulting catalyst reveals that iron sulfide nanoparticles are homogeneously embedded on the surface of reduced graphene oxide sheet. Electrochemical analysis of the hybrid exhibits remarkably improved catalytic performance for oxygen reduction reaction while achieving half wave potential of +0.845 V and onset potential of +1.0 V (*versus* reversible hydrogen electrode), along with outstanding long-term stability under alkaline conditions. In addition, the methanol tolerance ability and stability of the hybrid exceed the benchmark platinum/carbon product in alkaline condition. These outstanding activities of the hybrid are attributed to the merits of the interaction between iron sulfide nanoparticles and graphene. The results suggest the practicability of metal sulfide as a low cost and efficient alternative catalyst of platinum for oxygen reduction reaction.

1. Introduction

The increasing energy crisis and environmental threat produced by the excessive use of fossil fuels demand the commercialization of sustainable energy conversion and storage technologies like fuel cells, batteries, and supercapacitors … to reduce the dependency on fossil fuels [1,2]. Among them, the fuel cell is reliable energy conversion technology due to its high energy density, rapid start-up, zero emissions, environmental friendliness, and low operating temperature … [3–5]. Principally, the fuel cell generates electricity through an anodic and cathodic electrochemical reaction and the movement of ions from the anode to the cathode through the electrolyte, resulting in the flow of electrons via the external circuit [6]. Though fuel cell is simple, efficient, convenient, and eco-friendly energy conversion technology, it has several limitations. The critical drawback of fuel cells is the sluggish electron transfer rate of the oxygen reduction reaction (ORR) occurring at cathode, which is responsible for lowering the energy conversion

efficiency and is markedly influenced by the activity of cathodic catalyst [7]. Till now, platinum (Pt) is considered as the most reliable and efficient cathodic catalyst in fuel cells. However, Pt suffers the problems of high cost, easy poisoning, and instability [8–10]. Therefore, the development of highly efficient, durable, and cost-effective non-Pt catalysts for ORR is the focus of the commercialization in fuel cell technology.

In the past decades, various types of non-precious metal-based catalysts including transition metal oxides [11,12], transition metal sulfides (TMSs) [13], transition metal nitrides [14], and transition metal carbides … [15,16] have been widely pursued for electrocatalysis. Researchers have been examining the electrocatalytic properties of TMSs, such as Mo sulfides, Fe sulfides, Co sulfides, and Ni sulfides as candidates for energy conversion technologies, including dye-sensitized solar cells, batteries, capacitors, and catalysts for ORR. In particular, Fe sulfides have been emerging as promising candidates due to owning many exciting properties, including flexible bandgap, high coefficient of optical absorption, good carrier mobility, non-toxicity, and environmental
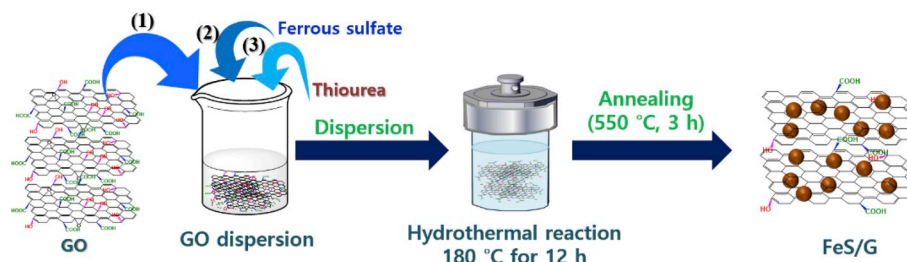
Scheme 1. Schematic diagram of the synthesis of the FeS/G hybrid.

compatibility [16]. Although these materials attracted particular interest, they also suffer from the problems of dissolution, sintering, and agglomeration during long-term operating condition of the fuel cells, which can result in the degradation of catalytic performance [17,18]. The low electrical conductivity of such materials is another problem, which significantly hampered the electron transport process during ORR [19]. Thus, a novel solution for preparing metal-based catalyst should be established to overcome these problems and expect high activity and stability towards ORR. In this regard, the combination of metal-based catalyst with highly conductive carbon supports has been becoming a promising way [20–22]. The reputation of supporting material has been well recognized by offering a large surface area for dispersing small catalyst particles, permitting mass transfer to/from electroactive sites, and accelerating charge conductivity within the active material layer. It has been pronounced that the design of catalyst via specific approaches with well-controlling conditions can critically affect the morphology, size, dispersion, and interaction of active metal with support, thereby minimizing shortcomings and maximizing the merits of the individual component to produce surprising catalytical activity and stability for electrochemical reactions [23–25]. Some hybrids based on Fe sulfides encapsulated multilayer structure of graphitic carbon (such as carbon nanotubes, carbon spheres …) have been reported; however, the number of exposed active sites, ion diffusion, electrolyte penetration may be

critically limited due to the hindrance of graphitic layers, thereby suggesting low ORR activity [26–28]. As an important carbon derivative, graphene has been receiving significant attraction because of its fascinating properties like extremely large specific area, outstanding thermal conductivity, high Young's modulus, good electrical conductivity, and charge mobility … [29–31]. Furthermore, the flexibility of graphene nanosheets can provide a large space to retain the metallic nanoparticle, which prevents agglomeration. Also, the good superficial characteristics and perfect structure of graphene improve the oxygen adsorption ability and electrical conductivity which significantly accelerates the electron transfer rate on the surface of graphene. Additionally, structural defects of graphene are responsible to create more active sites, which stimulates the ORR activity [32,33]. Therefore, iron sulfide/graphene hybrids have recently been considered for ORR. In a recent report by Fang et al., the developed Fe sulfide interpolated by reduced graphene oxide hybrids exhibited good efficiency for ORR in alkaline medium with positive onset potential (V_{on}) of +0.823 V *versus* reversible hydrogen electrode (vs. RHE) and good durability [34]; however, the use of co-precipitation synthesis method significantly limited the resulting material's performance due to the formation of big metal particle size with low dispersibility and significant agglomeration. In another research, Xiao et al., synthesized a raisin bread-structure of Fe sulfides with nitrogen and sulfur dual-doped graphitic layers of mesoporous carbon spheres via
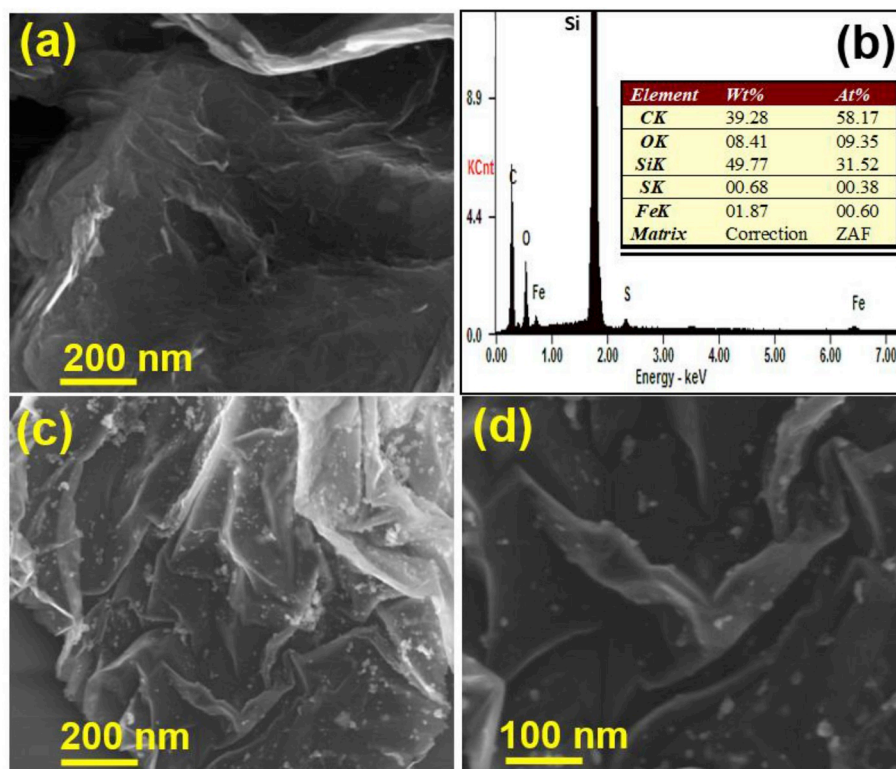

Fig. 1. (a) FE-SEM image of the rGO; (b) EDAX spectrum and (c, d) FE-SEM images of the FeS/G $_{(Fe/GO=1:4)}$ hybrid.
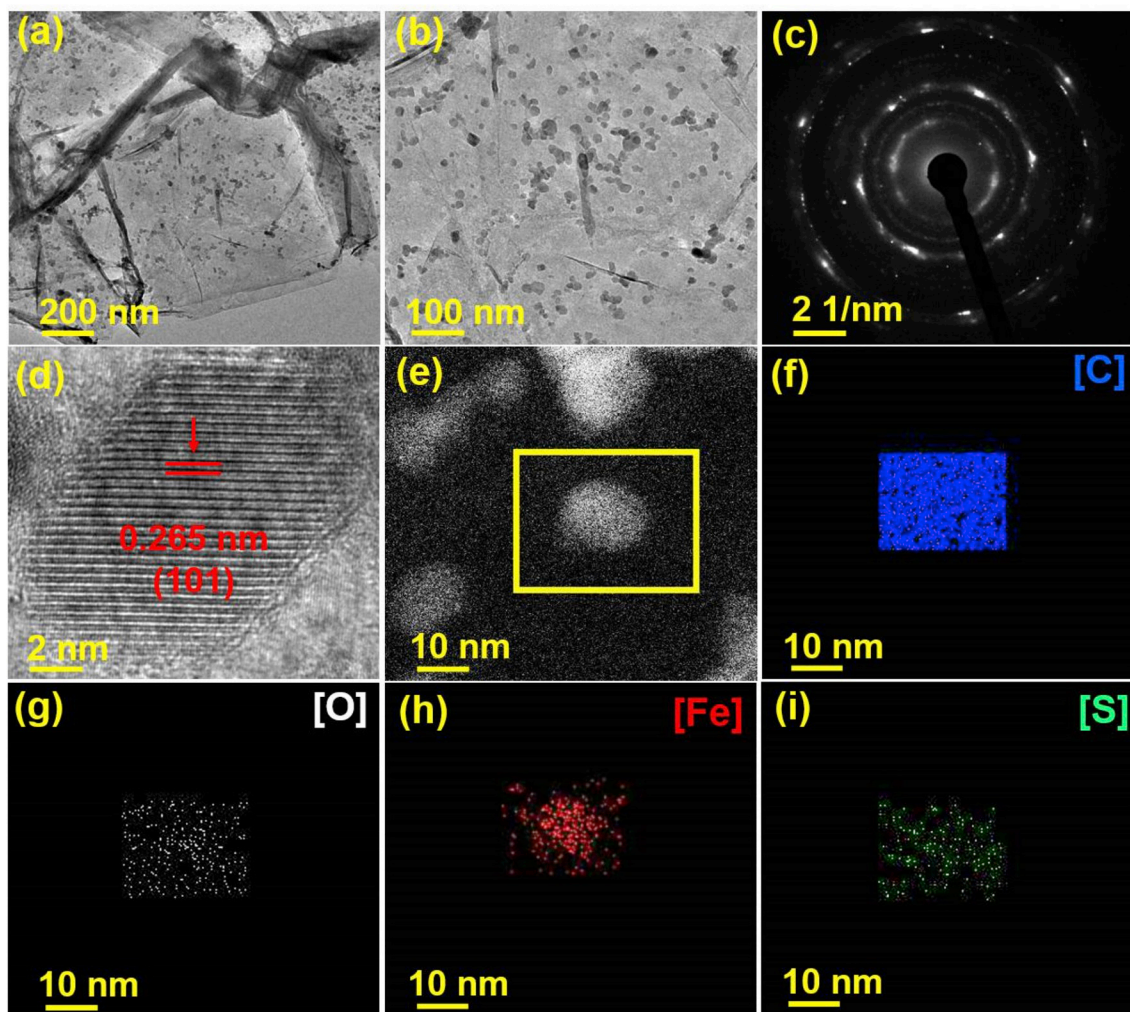
Fig. 2. (a, b) TEM images, (c) SAED pattern, and (d) HR-TEM image of the FeS/G$_{(Fe/GO=1:4)}$ hybrid (e–i); (e) STEM and its corresponding color mapping of a single particle in FeS/G$_{(Fe/GO=1:4)}$ hybrid. (For interpretation of the references to color in this figure legend, the reader is referred to the Web version of this article.)

a two-step pyrolysis and acid leaching process. In this context, the achieved catalyst also displayed promising electrocatalytic behavior for ORR, but the low graphitic degree and surface area of carbon spheres restricted charge transfer and dispersion of catalyst, thereby limiting reaction kinetics [35]. Although, some promising results have been pronounced for hybrid based on Fe sulfides and graphene, the publication about this hybrid system is rare and the above issues have not been addressed to improve activity and stability of catalyst towards ORR. Therefore, the design of a synthesis approach to effectively disperse small Fe sulfides on highly conductive and large-surface graphene nanosheets with enhanced synergistic effect is greatly necessary to improve ORR performance.

In this study, a hybrid based on Fe sulfides anchored graphene nanosheets was synthesized via a facile hydrothermal technique. The shape, size, morphology, and catalytic activity of the hybrid were optimized by altering the concentration of metal precursor and synthesis condition to maximize electroactive area, charge transfer ability, synergistic effects for modifying chemisorptive properties. The catalytic performance of the hybrid towards ORR in 0.1 M KOH was evaluated and compared with a commercial Pt/C product. In addition to a comparable catalytic activity, the resulting hybrid exhibited superior stability and methanol tolerance ability to the Pt/C. These results suggested that the synthesized hybrid could possess great cathodic catalyst for ORR in alkaline fuel cells.

2. Experimental

2.1. Materials

Graphite powder, ferrous sulfate heptahydrate (FeSO$_4$·7H$_2$O, 99.9%), potassium permanganate (KMnO$_4$, ≥99%), ammonia solution (NH$_3$.H$_2$O, ≥ 28%), commercial Pt/C catalyst (20 wt% of Pt), and nafion solution (5 wt %) were purchased from Sigma Co. (USA). Ethanol (C$_2$H$_5$OH, 99.9%), methanol (CH$_3$OH, 99.9%), hydrogen peroxide solution (H$_2$O$_2$, 30%), hydrochloric acid (HCl, (35–37) %), and potassium hydroxides (KOH, ≥ 99.5%) were purchased from Samchun Co. (South Korea).

2.2. Fabrication of FeS/G hybrid

In brief, graphene oxide (GO) (the synthesis procedure of GO is shown in the Supporting Information) dispersion was prepared by sonicating 0.04 g GO in a mixed solvent of 70 mL ethanol and 10 mL DI water for 1 h. Then, 0.24 g thiourea and 0.01 g ferrous sulfate were added to the solution under continuous magnetic stirring condition. The solution was subsequently transferred into a Teflon autoclave for hydrothermal treatment at 180 °C for 12 h. The precipitate obtained after the hydrothermal reaction was cleaned with ethanol/DI water several times, followed by freeze-drying and annealing in N$_2$ environment at 550 °C for 3 h, to produce FeS/G $_{(Fe/GO=1:4)}$ hybrid. Scheme 1 shows the
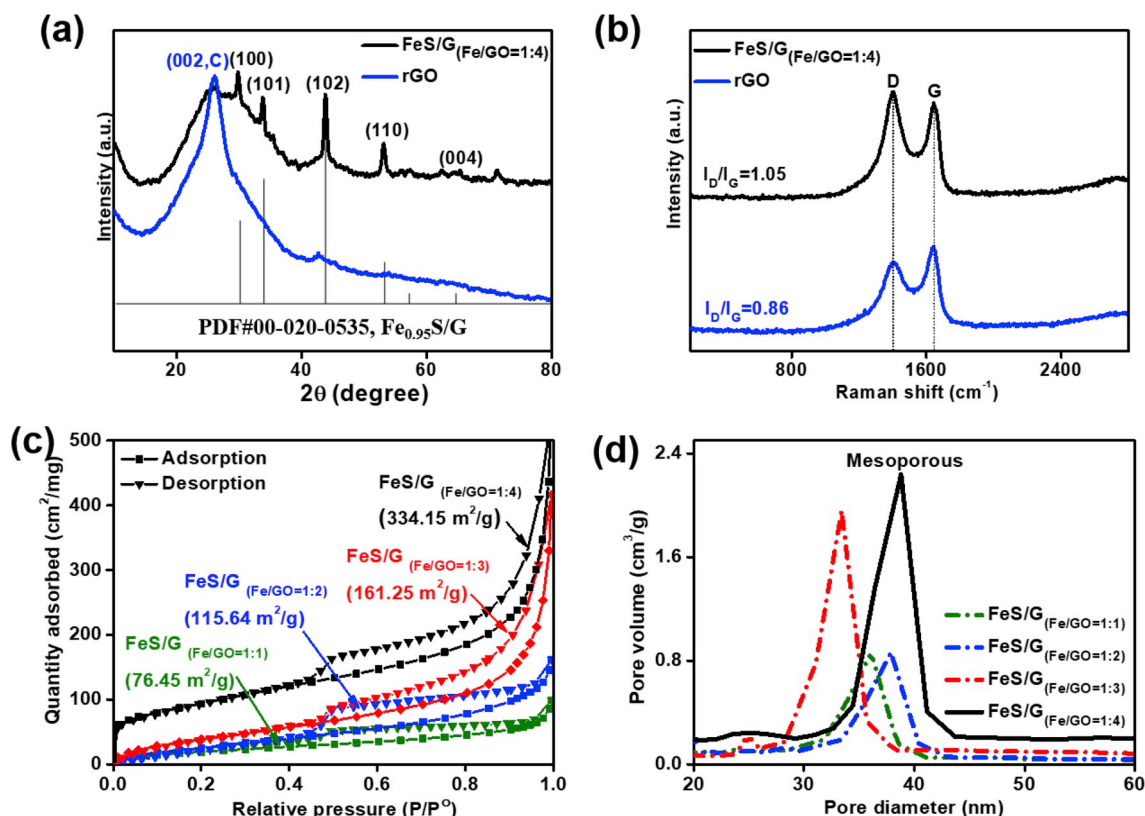
Fig. 3. (a) XRD spectra of the rGO and FeS/G$_{(Fe/GO=1:4)}$; (b) Raman spectra of the rGO and FeS/G $_{(Fe/GO=1:4)}$; (c) BET surface area and (d) pore size distribution of different FeS/G hybrid samples.

synthesis process of the FeS/G $_{(Fe/GO=1:4)}$ hybrid. For comparison, other FeS/G hybrids with different concentrations of Fe^{2+} precursor were also prepared under identical hydrothermal reaction and annealing step.

2.3. Characterization

The surface morphology and microstructure of the resulting hybrid were studied by field emission scanning electron microscopy (FE-SEM) on a Supra 40 VP instrument (Zeiss Co., Germany) and transmission electron microscopy (TEM) on a JEM-2200FS system (JEOL Co., USA) situated at the Korea Basic Science Institute at Chonbuk National University (Jeonju). Powder X-ray diffraction (XRD) patterns were checked on a Max 2500V/PC (Rigaku Co., Japan) at the Center for University-Wide Research Facilities (CURF), Chonbuk National University, using a Cu-K$_\alpha$ target ($\lambda = 0.154$ nm) in the 2θ range of (5–80)° at a scan rate of 2 °C·min^{-1}. Raman spectra were recorded from the Nanofinder® 30 (Tokyo Instruments Co., Japan). The chemical composition of catalyst was analyzed by X-ray photoelectron spectroscopy (XPS) on a Theta Probe machine (Thermo Fisher Scientific Inc., USA). The specific surface area was evaluated by the ASAP 2020 Plus system (Micromeritics Instrument Corp., USA), on the basis of Brunauer-Emmett-Teller (BET) theory.

2.4. Electrochemical measurements

The oxygen reduction activity of the synthesized hybrid was evaluated by rotating ring-disk electrode rotator RRDE-3A (ALS Co., Japan) integrated with an electrochemical workstation CHI 660D (CH Instruments Inc., USA), where RDE (0.071 cm^2), Ag/AgCl electrode, and graphite rod were used as working, reference, and counter electrode, respectively. The working electrode was prepared by dispersing 2.5 mg powder of the hybrid in 0.5 mL of ethanol and 5 μL of Nafion (5 wt %) under sonication for 30 min. Then, 5 μL of the catalyst ink was dropped

on the clean surface of the RDE, followed by drying for 3 h at room temperature. For comparative study, the working electrode was also prepared for commercial Pt/C. The cyclic voltammetry (CV) was performed in 0.1 M KOH electrolyte saturated with N$_2$/O$_2$ gas at the potential window of +0.15–1.15 V (vs. RHE) at a scan rate of 50 mV s^{-1}. Linear sweep voltammetry (LSV) was performed in 0.1 M KOH electrolyte saturated with O$_2$ at different rotation rates of the RDE (such as 400, 800, 1200, 1600, and 2000 rpm) and at a scan rate of 10 mV s^{-1}. Electrochemical impedance spectroscopy (EIS) was measured at +0.86 V (vs. RHE) in the frequency range (10^{-1} to 10^6 Hz) along with a potential amplitude of 5 mV. The mechanism of the reaction, kinetics, and the number of electrons transferred were calculated from the Koutecky-Levich (K-L) equations at various applied potentials [36]:

$$\frac{1}{J} = \frac{1}{j_L} + \frac{1}{j_K} = \frac{1}{B\omega^{1/2}} + \frac{1}{j_K} \tag{1}$$

$$B = 0.62nFC_oD_o^{2/3}v^{-1/6} \tag{2}$$

where, J, J$_K$, and J$_L$ are the observed current density (mA·cm^{-2}), kinetic-limiting current density (mA cm^{-2}), and diffusion-limiting current density (mA·cm^{-2}), respectively; ω is the rotation speed of the electrode (rad·s^{-1}); n is the electron transfer number; F is the Faraday constant (F = 96,485 C mol^{-1}); D$_O$ is the coefficient of diffusion of oxygen gas (D$_O$ = 1.9 × 10-5 cm^2 s^{-1}); C$_O$ is the saturated oxygen concentration in the 0.1 M KOH solution (C$_O$ = 1.2 × 10^{-6} mol cm^{-3}); and ν is the kinematic viscosity, which is equal to 0.01 cm^2 s^{-1}.

The 3 M methanol (MeOH) tolerance ability of the catalyst was analyzed by chronoamperometry in O$_2$-saturated 0.1 M KOH solution at a rotation speed of 1600 rpm and an applied potential of +0.66 V (vs. RHE). The durability was performed by chronoamperometry in O$_2$-saturated 0.1 M KOH at a rotation speed of 1600 rpm and an applied potential of +0.66 V (vs. RHE) for 20,000 s.
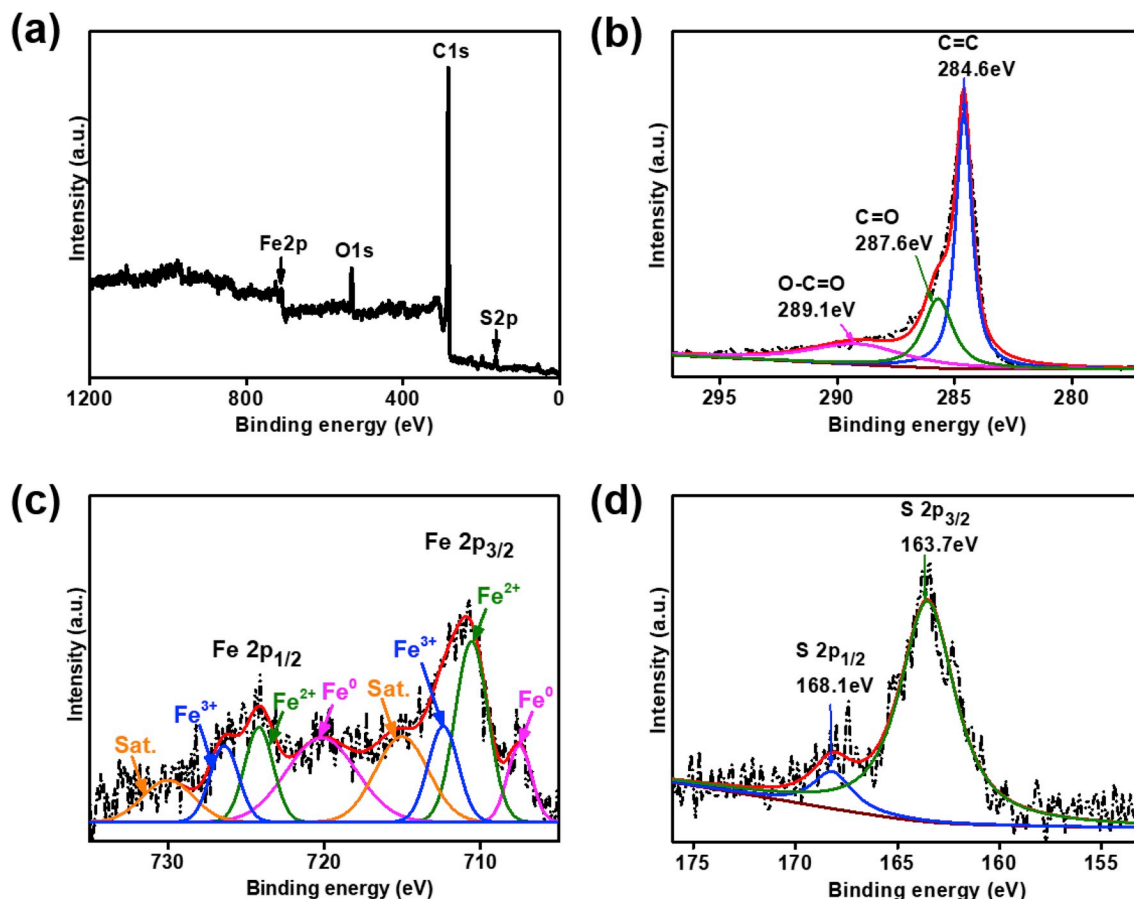
Fig. 4. (a) The surveyed XPS spectrum of the FeS/G$_{(Fe/GO=1:4)}$ hybrid and high-resolution XPS spectra of (b) C1s, (c) Fe2p and (d) S2p from FeS/G$_{(Fe/GO=1:4)}$ hybrid.

All recorded potentials were converted into the scale of the reversible hydrogen electrodes (RHE) by following equation

$$E_{RHE} = E_{Ag/AgCl} + 0.059\ pH + E°_{Ag/AgCl}\ (E°_{Ag/AgCl} = 0.1976V\ at\ 25\ °C)$$

3. Results and discussion

Scheme 1 illustrates the fabrication process of the FeS/G $_{(Fe/GO=1:4)}$ hybrid. Firstly, Fe^{2+} ions are absorbed on the surface of GO sheet via electrostatic interactions. Then, thiourea is broken down under hydrothermal condition at 180 °C to release H_2S, which reacted with Fe^{2+} ions to form FeS nanocrystals, as presented in the following reaction steps (1)–(2):

$$(NH_2)_2CS + 2H_2O = CO_2 + H_2S + 2NH_3 \qquad (3)$$

$$Fe^{2+} + S^{2-} = FeS \qquad (4)$$
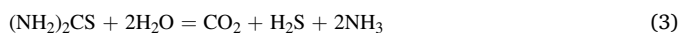
The formation of FeS crystals depends strongly on the surfactants, pH value, and the content of the S precursor present in the reaction system [37,38]. It has been reported that excess sulfur content favors the formation of well-defined FeS nanoparticles (NPs) and the use of surfactants as a capping agent favors the formation of truncated corners [39]. At this moment, GO with many chemical functional groups, such as –CO, –COOH, and –OH, acts both as a surfactant and accelerator, which promote the hydrolytic cleavage of $(NH_2)_2CS$ to produce excess sulfur source for accelerating the formation of the FeS NPs via Ostwald ripening and ion exchange process. At the same time, GO sheets are also reduced by removing the chemical functional groups, such as –CO, –COOH and –OH from its structure under high temperature and

high-pressure hydrothermal conditions [40]. The uniform formation of the FeS NPs on the large surface of the reduced GO (rGO) can effectively avoid both restacking of graphene sheets and aggregation of the NPs, thereby expecting to the change of intrinsic characteristic promising for electrochemical reaction [41].

To analyze the surface morphology and microstructure of the synthesized rGO and FeS/G$_{(Fe/GO=1:4)}$ hybrid, FE-SEM and TEM techniques were employed. The FE-SEM image of the rGO (Fig. 1a) shows some wrinkles and ripples on its surface, suggesting its highly reduced features [42]. Fig. 1b shows the EDAX spectrum of the FeS/G$_{(Fe/GO=1:4)}$ hybrid with the presence of respective elements, including C (58.17 at %), O (9.35 at%), Fe (0.6 at%), and S (0.38 at%). FE-SEM images of the hybrid at different magnifications (Fig. 1c to d) display the uniform distribution of the FeS NPs (∼5–10 nm) on the whole surface of the rGO sheet, further demonstrating the effectiveness of present synthesis method to produce hybrids of FeS NPs and graphene. The elemental composition of the hybrid was further evaluated by SEM-EDS color mapping analysis (Fig. S1), which demonstrates the homogeneous mixing of Fe and S atom throughout the entire surface of the graphene.

The detail information of the surface morphology and internal structure for the FeS/G $_{(Fe/GO=1:4)}$ hybrid was studied by TEM and high resolution (HR)-TEM analysis. TEM images (Fig. 2a and b) show the similar morphology to that observed by FE-SEM, in which 5–10 nm sized FeS NPs are uniformly anchored on the graphene sheet. The SAED pattern (Fig. 2c) of the hybrid suggests the highly crystalline feature of the FeS NPs. The HR-TEM image of the hybrid (Fig. 2d) displays the clearly distinguishable lattice fringe, consistent with a spacing of 0.265 nm, which agrees with the d(101) crystal plane from $Fe_{0.95}S$ (JCPDS card no. 20–0535). In addition, the result of EDS color mapping for a single particle (Fig. 2e–i) further depict the anchorage of the FeS NP on the surface of graphene.
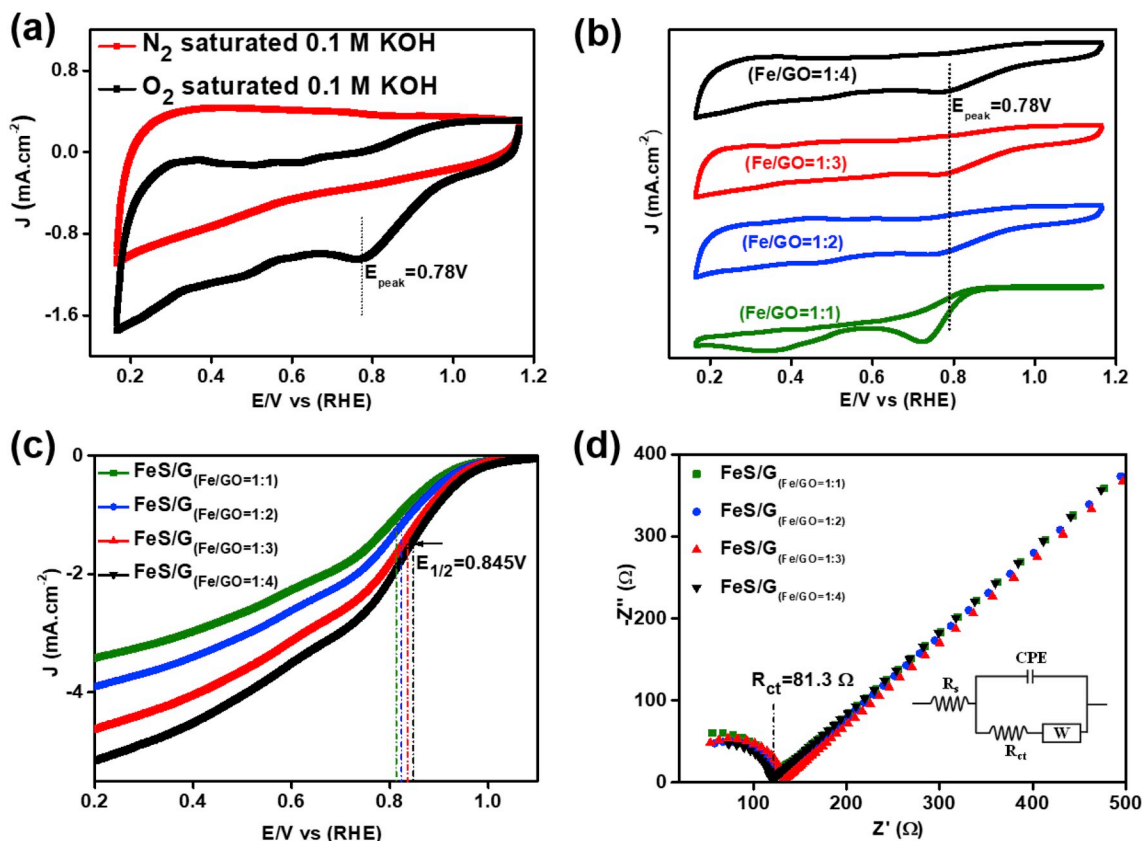
Fig. 5. (a) CV curves of the FeS/G$_{(Fe/GO=1:4)}$ hybrid in N$_2$- and O$_2$-saturated 0.1 M KOH electrolyte; (b) Comparison of ORR activity of different FeS/G hybrids in 0.1 M KOH electrolyte; (c) LSV of different FeS/G hybrids in 0.1 M KOH electrolyte at a rotation speed of 1600 rpm and a scan rate of 10 mV·s^{-1}; (d) EIS results of different FeS/G hybrids in 0.1 M KOH electrolyte in the frequency range of 10^5 to 10^{-2}.

The crystallinity of the FeS NPs anchored on rGO sheets was examined by XRD analysis. The XRD spectrum of the FeS/G$_{(Fe/GO=1:4)}$ (Fig. 3a) shows a broad peak at 2θ ≈ 26°, corresponding to the d(002) crystal plane of graphitic structure [43]. The presence of diffraction peaks at 2θ ≈ 29.9°, 33.8°, 43.85°, and 53° is attributed to the crystal planes of the d(100), d(101), d(102), and d(110) faces from Fe$_{0.95}$S (JCPDS card no. 20–0535), fully consistent with the TEM results. In addition, the intensity of the diffraction peaks for the FeS/G$_{(Fe/GO=1:4)}$ hybrid is higher than those of the other synthesized FeS/G samples, suggesting a better crystallinity of the FeS NPs in such hybrid (Figs. 3a and S3b). The XRD analysis indicates that the highly crystalline FeS NPs are anchored on rGO sheet, in which rGO played a vital role to prevent the aggregation of the FeS NPs.

From another aspect, Raman analysis was performed to investigate the surface defects of the graphitic structure in the FeS/G$_{(Fe/GO=1:4)}$ hybrid and rGO. Raman spectra of two samples (Fig. 3b) display two obvious peaks at 1340 and 1590 cm^{-1}, which are consistent with D and G band of graphitic carbon, respectively. The D band informs the disordered states and the G band signifies the stretching vibration mode E$_{2g}$ from sp^2 bonded pairs. The ratio of D-to-G band (I$_D$/I$_G$) can be used as a useful indicator for evaluating the defects in graphitic carbon materials. In this regard, the I$_D$/I$_G$ ratio is observed to be about 1.05 and 0.86 for FeS/G$_{(Fe/GO=1:4)}$ hybrid and rGO, respectively. As compared to rGO and the other synthesized FeS/G samples (Figs. 3b and S3a), the higher I$_D$/I$_G$ value of the FeS/G$_{(Fe/GO=1:4)}$ indicates that additional defects were introduced into the surface of the graphene via the surface modification and the anchorage of FeS NPs [44]. Nitrogen adsorption-desorption isotherms and Brunauer-Emmett-Teller (BET) analysis were employed to check the porosity and specific surface area of the FeS/G$_{(Fe/GO=1:4)}$ hybrid. The N$_2$ adsorption-desorption isotherms exhibit a typical hysteresis loop of type IV, suggesting the mesoporous

features of such hybrid (Fig. 3c). The BET analysis indicates the highest specific surface area of the FeS/G$_{(Fe/GO=1:4)}$ hybrid (334.15 m^{2}g^{-1}) as compared to other FeS/G hybrid samples. In addition, mesoporous nature of the hybrids is further demonstrated by Fig. 3d, which shows the pore size of the hybrids is mainly concentrated in the range of 30–40 nm. The large surface area and mesoporous nature of the catalysts are expected to be highly beneficial for enhancing catalytic activity via offering more active sites, diverse ion/electron conduction pathways, and reactant diffusion channels … [45,46].

The chemical composition and bonding states of the FeS/G$_{(Fe/GO=1:4)}$ hybrid were analyzed by XPS technique. The survey XPS spectrum (Fig. 4a) shows the presence of C, O, Fe, and S elements in the hybrid, in which the signal of C and O is originated from the rGO sheets [47] and the signal of Fe and S is from FeS NPs. The high-resolution C1s spectrum of the hybrid can be deconvoluted into three peaks (Fig. 4b), which are attributed to C=C (284.6 eV), C=O (287.6 eV), and O-C=O (289.1 eV) of the rGO. As compared to the GO material, the different types of functional groups in the C1s spectrum of the FeS/G$_{(Fe/GO=1:4)}$ hybrid are disappeared (Fig. 4b and Table S1), indicating the well reduced features of the GO in the synthesized hybrid [48,49]. The high-resolution Fe2p spectrum shows four doublets, which are attributed to the binding energies of Fe^0, Fe^{2+}, Fe^{3+}, and satellite component (Fig. 4c) [34]. In this context, two peaks at 707.3 and 720.3 eV, consistent with 2p3/2 and 2p1/2 levels of Fe^0, respectively. Besides, the peaks at 710.6 and 724.2 eV are assigned to Fe^{2+}, and the peaks at 712.4 and 726.5 eV are corresponding to Fe^{3+}, revealing the presence of both Fe^{3+} and Fe^{2+} in the FeS/G hybrid [50]. The peaks at 715.1 and 730.0 eV respectively belong to satellite component of Fe2p3/2 and Fe2p1/2 [51]. Regarding the high-resolution S2p spectrum of the hybrid, the characteristic peaks of S2p1/2 and S2p3/2 are detected at binding energies of 168.1 and 163.7 eV (Fig. 4d), respectively, consistent with characteristics of S^{2-}
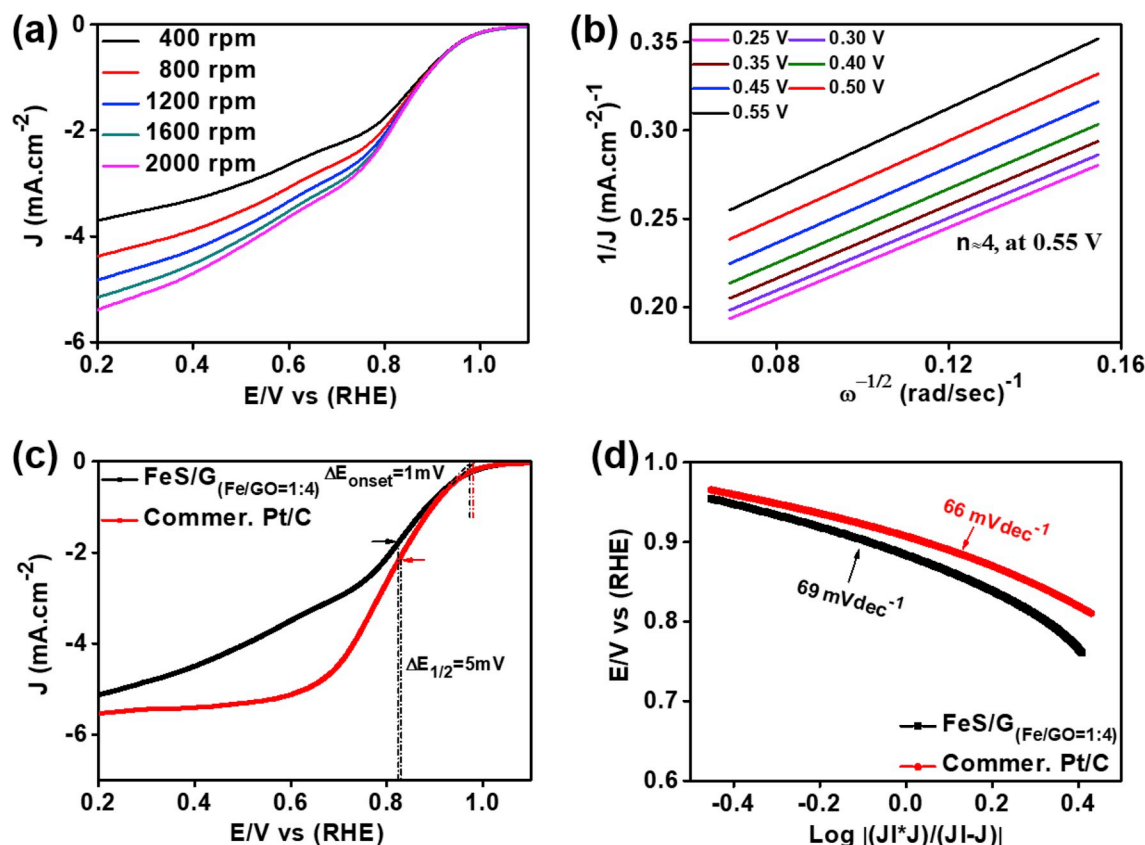
Fig. 6. (a) LSV curve of the FeS/G$_{(Fe/GO=1:4)}$ hybrid at a scan rate of 10 mV·s^{-1} in O$_2$-saturated 0.1 M KOH electrolyte at different rotation rates of the electrode; (b) Plot of J^{-1} vs ω$^{-1/2}$ according to the K–L equation at different applied potentials for FeS/G$_{(Fe/GO=1:4)}$ hybrid; (c) LSV comparison and (d) the corresponding Tafel plot comparison of the FeS/G$_{(Fe/GO=1:4)}$ hybrid with Pt/C at 1,600 rpm in 0.1 M KOH.

[52].

The ORR activity of the FeS/G hybrids was initially evaluated by CV measurement in N$_2$ and O$_2$-saturated 0.1 M KOH electrolyte. Fig. 5a shows that the CV curve of the FeS/G$_{(Fe/GO=1:4)}$ hybrid exhibits distinguished cathodic peak at +0.78 V (vs. RHE) in O$_2$-saturated KOH, suggesting the superior catalytic activity of such catalyst towards ORR in survey potential range. Also, the CV comparison of different FeS/G hybrids with varying ratio of iron salt precursor in O$_2$-saturated 0.1 M KOH solution shows the maximum peak current density and most positive peak potential (E$_{peak}$ = 0.78V (vs. RHE)) for the FeS/G$_{(Fe/GO=1:4)}$ hybrid (Fig. 5b). The LSV comparison also demonstrates the similar result to CV, in which the highest value of onset potential (V$_{onset}$), half-wave potential (V$_{half\ wave}$), and the measured current density were obtained for the FeS/G$_{(Fe/GO=1:4)}$ hybrid (with V$_{onset}$ = 1.0 V and V$_{half\ wave}$ = 0.845 V (vs. RHE)), informing the high catalytic activity of the catalyst as compared to other FeS/G hybrid samples (Fig. 5c).

EIS measurements were also performed to evaluate the charge transfer resistance of different FeS/G hybrids. Fig. 5d shows the smallest semicircle, consistent with the lowest R$_{ct}$ value for FeS/G$_{(Fe/GO=1:4)}$ (102.5 Ω), as compared to other catalysts, suggesting its high electron transfer ability for ORR. The good catalytic performance and high electron transfer ability of the FeS/G$_{(Fe/GO=1:4)}$ hybrid are attributed to the synergistic effects originated from the uniform attachment of the FeS NPs on graphene's surface, as observed in FE-SEM and TEM images. The uniform distribution of the FeS NPs leads to the enhancement of surface area, conductivity, active sites numbers on the surface of graphene, thereby upgrading the interfacial charge transfer ability and O$_2$ adsorption ability to amplify the electrocatalytic activity of the catalyst [53].

To explore the kinetics and mechanism of ORR, the LSV measurements were investigated in O$_2$-saturated 0.1 M KOH solution at different

rotation speeds (Fig. 6a). The current density consistently increases with the rotation speed, which is due to the shortened distance of electron transport channel between the electrolyte-electrode interface, suggesting the significant impact of kinetic factors on ORR activity. To study the mechanism of electron transfer, Koutecky-Levich (K-L) plot were made for the FeS/G$_{(Fe/GO=1:4)}$ in the potential range (0.25–0.5 V (vs. RHE)). The achieved K-L plots of the FeS/G$_{(Fe/GO=1:4)}$ show good linearity and parallelism in the measured potential range, signifying similar electron transfer mechanism and the first order reaction kinetics of the catalyst towards ORR [54,55]. In addition, electron transfer number (n) value obtained from the K-L plots at potential of +0.55 V (vs. RHE) was ~4.0 (Figs. 6b and S6) for FeS/G$_{(Fe/GO=1:4)}$, which was higher than the electron transfer number of other catalysts, suggesting the ORR catalyzed by this hybrid was mainly occurred through the direct 4 electrons transfer pathway without involving any intermediate steps. In order to check the appropriateness of the catalyst for practical application, the catalytic activity of the catalyst was compared with the commercial Pt/C by LSV measurements in O$_2$-saturated 0.1 M KOH at a rotation speed of 1600 rpm. The LSV comparison shows that the catalytic activity of the FeS/G$_{(Fe/GO=1:4)}$ hybrid is almost like Pt/C. In this regard, the hybrid presents slightly lower value of V$_{onset}$ (1 mV) and V$_{half\ wave}$ (5 mV) as compared to Pt/C (Fig. 6c).

In addition, the Tafel slope comparison also suggests the similar catalytic activity and overpotential of the FeS/G$_{(Fe/GO=1:4)}$ hybrid (69 mV·dec^{-1}) with Pt/C (66 mV·dec^{-1}) catalyst towards ORR, indicating the high feasibility of the hybrid for practical applications (Fig. 6d). To the best of our knowledge, the FeS/G$_{(Fe/GO=1:4)}$ hybrid has displayed excellent catalytic activity towards ORR in 0.1 M KOH solution compared to the formerly reported metal sulfide-based catalyst (Table S2).

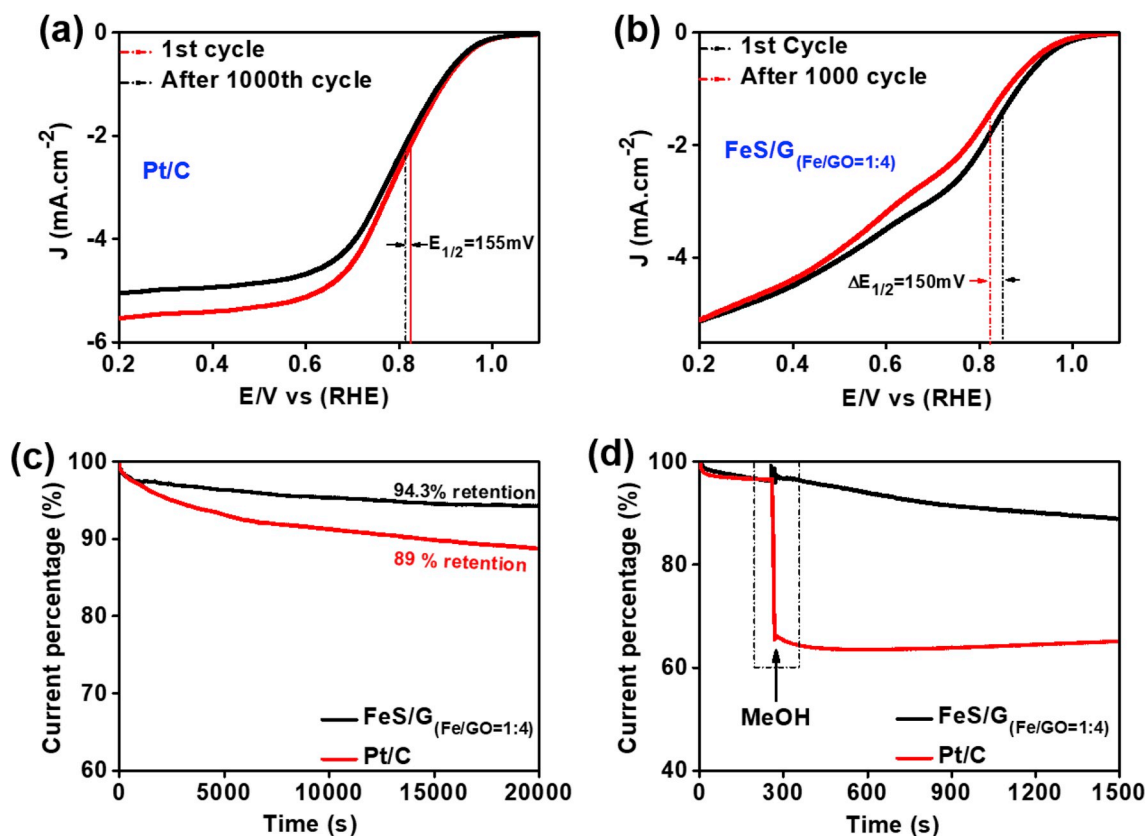The durability and methanol tolerance ability of the catalyst are also

Fig. 7. (a) LSV comparison of Pt/C and (b) FeS/G$_{(Fe/GO=1:4)}$ hybrid in O$_2$-saturated 0.1 M KOH at 1600 rpm after consecutive run of 1,000th cycles; (c) Chronoamperometric measurements (i-t curve) of the FeS/G$_{(Fe/GO=1:4)}$ hybrid and Pt/C in O$_2$-saturated 0.1 M KOH electrolyte at an applied potential of +0.66 V (vs. RHE) and rotation rate of 1600 rpm for 20,000 s; (d) Comparative study of MeOH tolerance ability of the FeS/G$_{(Fe/GO=1:4)}$ hybrid and Pt/C by chronoamperometry at +0.66 V (vs. RHE) in O$_2$ saturated 0.1 M KOH at 1600 rpm.

vital parameters to determine its practical ability towards ORR. In order to examine the durability of the catalyst, LSV comparisons were made between FeS/G$_{(Fe/GO=1:4)}$ hybrid and Pt/C after a consecutive run of 1000 cycles at a scan rate of 50 mV·s^{-1} in O$_2$-saturated 0.1 M KOH electrolyte at 1600 rpm. The LSV curve of the Pt/C displays a 155 mV deflection of V$_{half wave}$ after 1000 cycles (Fig. 7a), meanwhile the FeS/G$_{(Fe/GO=1:4)}$ hybrid displays only 150 mV loss in V$_{half wave}$ after 1000 potential cycles (Fig. 7b), implying the greater stability for FeS/G$_{(Fe/GO=1:4)}$ as compared to the Pt/C. To further confirm the enhanced stability of the FeS/G$_{(Fe/GO=1:4)}$ hybrid, the chronoamperometry at a constant voltage of +0.66 V (vs. RHE) for 20,000 s was compared between FeS/G$_{(Fe/GO=1:4)}$ hybrid and Pt/C catalyst (Fig. 7c). The results show the excellent retention of the current density for FeS/G$_{(Fe/GO=1:4)}$ hybrid (94.3%), as compared to that of Pt/C (89%), demonstrating the superior stability of the hybrid catalyst. The morphology and structure of the FeS/G and Pt/C after stability test were investigated to deeply understand certain reason for the observed stability of these materials. Fig. S8a indicates the respectable preservation of FeS/G morphology, in which FeS NPs still well distribute over surface of the G. In addition, Fig. S8b shows that there is no significant change of crystal structure for the hybrid. These observations are fully consistent with the good stability of the hybrid material towards ORR. In contrast, the reduction of stability for the Pt/C was demonstrated by the considerable decomposition of its structure, in which TEM image of Pt/C after stability clearly displays a strong decrease of Pt density on carbon surface because of the dissolution and detachment during operation (Figs. S9a and b). In addition, the XRD result of Pt/C after stability also shows low intensity and broaden diffraction peaks as compared to virgin one, further implying significant modulation of Pt structure (Fig. S9c), thereby leading to the impressive reduction of stability towards ORR.

In addition to the high activity and durability, the FeS/G$_{(Fe/GO=1:4)}$ hybrid also possesses excellent methanol tolerance ability towards ORR. In this regard, the methanol tolerance ability of the FeS/G$_{(Fe/GO=1:4)}$ and Pt/C was evaluated by chronoamperometry at +0.66 V (vs. RHE) in 0.1 M KOH solution. It can be seen that after injecting 3 M methanol at 300 s time point (Fig. 7d), the Pt/C catalyst presents a sharp and immediate jumping in current density, whereas a minor change is only noticed in the case of the FeS/G$_{(Fe/GO=1:4)}$ hybrid. This infers the superior MeOH tolerance ability of the hybrid catalyst to Pt/C [56,57]. All above electrochemical results excitingly suggest the excellent catalytic activity, high stability, and high methanol tolerance ability of the FeS/-G$_{(Fe/GO=1:4)}$ hybrid towards ORR in 0.1 M KOH solution, demonstrating its great feasibility for replacing Pt/C catalyst.

4. Conclusion

In summary, a novel and cost-effective catalyst based on FeS/G hybrid is successfully fabricated through hydrothermal technique and efficiently applied for ORR in alkaline medium. The comparison of electrocatalytic activity for different FeS/G hybrid samples reveals that FeS/G$_{(Fe/GO=1:4)}$ hybrid exhibits excellent catalytic activity with positive V$_{onset}$, V$_{half-wave}$, cycling stability, and MeOH tolerance ability. The hybrid shows a close catalytic performance, as well as superior stability and methanol tolerance to Pt/C catalyst. The superb catalytic activity of the optimized FeS/G catalyst is basically attributed to the synergistic effect of FeS NPs and graphene, which produce large surface area, enhanced active site numbers, and numerous channels for ion/electrolyte diffusion. Such factors are vital for improving charge conductivity and O$_2$ adsorption ability to enhance the catalytic activity towards ORR. All results demonstrated the practical ability of the FeS/G$_{(Fe/GO=1:4)}$

hybrid to replace commercial Pt/C for ORR in alkaline medium.

Acknowledgements

Appendix A. Supplementary data

Supplementary data to this article can be found online at https://doi.org/10.1016/j.jpowsour.2019.04.075.

References

[1] W.R.W. Daud, R.E. Rosli, E.H. Majlan, S.A.A. Hamid, R. Mohamed, T. Husaini, PEM fuel cell system control: a review, Renew. Energy 113 (2017) 620–638.

[2] V. Das, S. Padmanaban, K. Venkitusamy, R. Selvamuthukumaran, F. Blaabjerg, P. Siano, Recent advances and challenges of fuel cell-based power system architectures and control – a review, Renew. Sustain. Energy Rev. 73 (2017) 10–18.

[3] G. Wang, Y. Yu, H. Liu, C. Gong, S. Wen, X. Wang, Z. Tu, Progress on design and development of polymer electrolyte membrane fuel cell systems for vehicle applications: a review, Fuel Process. Technol. 179 (2018) 203–228.

[4] M.K. Debe, Electrocatalyst approaches and challenges for automotive fuel cells, Nature 486 (2012) 43–51.

[5] I.E.L. Stephens, J. Rossmeisl, I. Chorkendorff, Toward sustainable fuel cells, Science 354 (2016) 1378–1379.

[6] O.Z. Sharaf, M.F. Orhan, An overview of fuel cell technology: fundamentals and applications, Renew. Sustain. Energy Rev. 32 (2014) 810–853.

[7] S. Sui, X. Wang, Y. Su, X. Zhou, S. Riffat, C.J. Liu, A comprehensive review of Pt electrocatalysts for the oxygen reduction reaction: nanostructure, activity, mechanism and carbon support in PEM fuel cells, J. Mater. Chem. A 5 (2017) 1808–1825.

[8] Z. Xiang, Y. Xue, D. Cao, L. Huang, J.F. Chen, L. Dai, Highly efficient electrocatalysts for oxygen reduction based on 2D covalent organic polymers complexed with non-precious metals, Angew. Chem. Int. Ed. 53 (2014) 2433–2437.

[9] D. Yan, Y. Li, J. Huo, R. Chen, L. Dai, S. Wang, Defect chemistry of nonprecious-metal electrocatalysts for oxygen reactions, Adv. Mater. 29 (2017) 1606459.

[10] Y. Hu, J.O. Jensen, S. Martin, W. Zhang, C. Pan, R. Chenitz, Wei Xing, N.J. Bjerrum, Q. Li, Fe_3C-based oxygen reduction catalysts: synthesis, hollow spherical structures and applications in fuel cells, J. Mater. Chem. A 3 (2015) 1752–1760.

[11] H. Osgood, S.V. Devaguptapu, H. Xu, J. Cho, G. Wu, Transition metal (Fe, Co, Ni, and Mn) oxides for oxygen reduction and evolution bifunctional catalysts in alkaline media, Nano Today 11 (2016) 601–625.

[12] D.T. Tran, T. Kshetri, D.C. Nguyen, J. Gautam, V.H. Hoa, H.T. Le, N.H. Kim, J. H. Lee, Emerging core-shell nanostructured catalysts of transition metal encapsulated by two-dimensional carbon materials for electrochemical applications, Nano Today 22 (2018) 100–131.

[13] T.D. Thanh, N.D. Chuong, H.V. Hien, T. Kshetri, N.H. Kim, J.H. Lee, Recent advances in two-dimensional transition metal dichalcogenides-graphene heterostructured materials for electrochemical applications, Prog. Mater. Sci. 96 (2018) 51–85.

[14] T. Sun, Q. Wu, R. Che, Y. Jiang, Y. Bu, L. Yang, Y. Li, X. Wang, Z. Hu, Alloyed Co−Mo nitride as high-performance electrocatalyst for oxygen reduction in acidic medium, ACS Catal. 5 (2015) 1857–1862.

[15] Y. Zhong, X. Xia, F. Shi, J. Zhan, J. Tu, H.J. Fan, Transition metal carbides and nitrides in energy storage and conversion, Adv. Sci. 3 (2016) 1500286.

[16] S.-Y. Huang, D. Sodano, T. Leonard, S. Luiso, P.S. Fedkiw, Cobalt-doped iron sulfide as an electrocatalyst for hydrogen evolution, J. Electrochem. Soc. 164 (2017) F276–F282.

[17] X. Li, G. Liu, B.N. Popov, Activity and stability of non-precious metal catalysts for oxygen reduction in acid and alkaline electrolytes, J. Power Sources 195 (2010) 6373–6378.

[18] C. Zhu, S. Dong, Recent progress in graphene-based nanomaterials as advanced electrocatalysts towards oxygen reduction reaction, Nanoscale 5 (2013) 1753–1767.

[19] A. Arunchander, S.G. Peera, A.K. Sahu, Self-assembled manganese sulfide nanostructures on graphene as an oxygen reduction catalyst for anion exchange membrane fuel cells, Chem. Electro. Chem. 4 (2017) 1544–1553.

[20] M. Sun, Y. Liu, H. Liu, J. Qu, J. Li, Graphene-based transition metal oxide nanocomposites for the oxygen reduction reaction, Nanoscale 7 (2015) 1250–1269.

[21] R. Chen, J. Yan, Y. Liu, J. Li, Three-dimensional nitrogen-doped graphene/mno nanoparticle hybrids as a high-performance catalyst for oxygen reduction reaction, J. Phys. Chem. C 119 (2015) 8032–8037.

[22] L. Dai, M. Liu, Y. Song, J. Liu, F. Wang, Mn_3O_4-decorated Co_3O_4 nanoparticles supported on graphene oxide: dual electrocatalyst system for oxygen reduction reaction in alkaline medium, Nanomater. Energy 27 (2016) 185–195.

[23] A. Arunchander, S.G. Peera, V.V. Giridhar, A.K. Sahu, Synthesis of cobalt sulfide-graphene as an efficient oxygen reduction catalyst in alkaline medium and its application in anion exchange membrane fuel cells, J. Electrochem. Soc. 164 (2017) 71–80.

[24] H. Wang, Y. Liang, Y. Li, H. Dai, $Co_{1-x}S$–graphene hybrid: a high-performance metal chalcogenide electrocatalyst for oxygen reduction, Angew. Chem. 123 (2011) 11161–11164.

[25] H. Liang, C. Li, T. Chen, L. Cui, J. Han, Z. Peng, J. Liu, Facile preparation of three-dimensional $Co_{1-x}S$/sulfur and nitrogen-codoped graphene/carbon foam for highly efficient oxygen reduction reaction, J. Power Sources 378 (2018) 699–706.

[26] L. Xu, Y. Hu, H. Zhang, H. Jiang, C. Li, Confined synthesis of FeS_2 nanoparticles encapsulated in carbon nanotube hybrids for ultrastable lithium-ion batteries, ACS Sustain. Chem. Eng. 4 (2016) 4251–4255.

[27] Y. Liu, W. Wang, Q. Chen, C. Xu, D. Ca, H. Zhan, Resorcinol–formaldehyde resin-coated prussian blue core–shell spheres and their derived unique yolk–shell FeS_2@ C spheres for lithium-ion batteries, Inorg. Chem. 58 (2019) 1330–1338.

[28] X. Ding, C. Du, J. Li, X. Huang, FeS_2 microspheres wrapped by N-doped rGO from an Fe-based ionic liquid precursor for rechargeable lithium ion batteries, Sustain. Energy Fuel. 3 (2019) 701–708.

[29] M. Hu, Z. Yao, X. Wang, Graphene-based nanomaterials for catalysis, Ind. Eng. Chem. Res. 56 (2017) 3477–3502.

[30] J. Li, H. Xie, Y. Li, J. Liu, Z. Li, Electrochemical properties of graphene nanosheets/polyaniline nanofibers composites as an electrode for supercapacitors, J. Power Sources 196 (2011) 10775–10781.

[31] D.K. Perivoliotis, N. Tagmatarchis, Recent advancements in metal-based hybrid electrocatalysts supported on graphene and related 2D materials for the oxygen reduction reaction, Carbon 118 (2017) 493–510.

[32] M. Liu, W. Chen, R. Zhang, Graphene-supported nano electrocatalysts for fuel cells: synthesis, properties, and applications, Chem. Rev. 114 (2014) 5117–5160.

[33] Q. Li, N. Mahmood, J. Zhu, Y. Hou, S. Sun, Graphene and its composites with nanoparticles for electrochemical energy applications, Nano Today 9 (2014) 668–683.

[34] H. Fang, T. Huang, J. Mao, S. Yao, M.M. Dinesh, Y. Sun, D. Liang, L. Qi, J. Yu, Z. Jiang, Investigation on the catalytic performance of reduced-graphene-oxide-interpolated fes[2] and fes for oxygen reduction reaction, Chem. Sel. 3 (2018) 10418–10427.

[35] J. Xiao, Y. Xia, C. Hu, J. Xi, S. Wang, Raisin bread-like iron sulfides/nitrogen and sulfur dual-doped mesoporous graphitic carbon spheres: a promising electrocatalyst for the oxygen reduction reaction in alkaline and acidic media, J. Mater. Chem. A 5 (2017) 11114–11123.

[36] T.D. Thanh, N.D. Chuong, H.V. Hien, N.H. Kim, J.H. Lee, CuAg@Ag core−shell nanostructure encapsulated by N-doped graphene as a high-performance catalyst for oxygen reduction reaction, ACS Appl. Mater. Interfaces 10 (2018) 4672–4681.

[37] X. Chen, Z. Wang, X. Wang, J. Wan, J. Liu, Y. Qian, Single-source approach to cubic fes_2 crystallites and their optical and electrochemical properties, Inorg. Chem. 44 (2005) 951–954.

[38] L. Zhu, B. Richardson, J. Tanumihardja, Q. Yu, Controlling morphology and phase of pyrite FeS_2 hierarchical particles via the combination of structure-direction and chelating agents, CrystEngComm 14 (2012) 4188–4195.

[39] D. Wang, Q. Wang, T. Wang, Controlled growth of pyrite FeS_2 crystallites by a facile surfactant-assisted solvothermal method, CrystEngComm 12 (2010) 755–761.

[40] Y. Zhou, Q. Bao, L.A.L. Tang, Y. Zhong, K.P. Loh, Hydrothermal dehydration for the "green" reduction of exfoliated graphene oxide to graphene and demonstration of tunable optical limiting properties, Chem. Mater. 21 (2009) 2950–2956.

[41] X. Wen, X. Wei, L. Yang, P.K. Shen, Self-assembled FeS_2 cubes anchored on reduced graphene oxide as an anode material for lithium ion batteries, J. Mater. Chem. A 3 (2015) 2090–2096.

[42] S. Radhakrishnan, K. Krishnamoorthy, C. Sekar, J. Wilson, S.J. Kim, A highly sensitive electrochemical sensor for nitrite detection based on Fe_2O_3 nanoparticles decorated reduced graphene oxide nanosheets, Appl. Catal. B Environ. 148 (2014) 22–28.

[43] S. Park, J. An, J.R. Potts, A. Velamakanni, S. Murali, R.S. Ruoff, Hydrazine-reduction of graphite and graphene oxide, Carbon 49 (2011) 3019–3302.

[44] W. Chen, S. Qi, L. Guan, C. Liu, S. Cui, C. Shen, L. Mi, Pyrite FeS_2 microspheres anchoring on reduced graphene oxide aerogel as an enhanced electrode material for sodium-ion batteries, J. Mater. Chem. A 5 (2017) 5332–5341.

[45] H. Chang, J. Kang, L. Chen, J. Wang, K. Ohmura, N. Chen, T. Fujita, H. Wu, M. Chen, Low-temperature solution-processable $Ni(OH)_2$ ultrathin nanosheet/N-graphene nanohybrids for high-performance supercapacitor electrodes, Nanoscale 6 (2014) 5960–5966.

[46] J. Gautam, T.D. Thanh, K. Maiti, N.H. Kim, J.H. Lee, Highly efficient electrocatalyst of N-doped graphene-encapsulated cobalt-iron carbides towards oxygen reduction reaction, Carbon 137 (2018) 358–367.

[47] Z. Zhang, Q. Wang, C. Zhao, S. Min, X. Qian, One-step hydrothermal synthesis of 3D petal-like Co_9S_8/RGO/Ni_3S_2 composite on nickel foam for high performance supercapacitors, ACS Appl. Mater. Interfaces 7 (2015) 4861–4868.

[48] D. Yang, A. Velamakanni, G. Bozoklu, S. Park, M. Stoller, R.D. Piner, S. Stankovich, I. Jung, D.A. Field, C.A. Ventrice, R.S. Ruoff, Chemical analysis of graphene oxide films after heat and chemical treatments by X-ray photoelectron and Micro-Raman spectroscopy, Carbon 47 (2009) 145–152.

[49] Y. Zhang, P. Ju, C. Zhao, X. Qian, In-situ grown of $MoS_2/RGO/MoS_2@Mo$ nanocomposite and its supercapacitor performance, Electrochim. Acta 219 (2016) 693–700.

[50] G.K. Veerasubramani, Y. Subramanian, M.-S. Park, G. Nagaraju, B. Senthilkumar, Y.-S. Lee, D.-W. Kim, Enhanced storage ability by using a porous pyrrhotite@N-doped carbon yolk–shell structure as an advanced anode material for sodium-ion batteries, J. Mater. Chem. A 6 (2018) 20056–20068.

[51] Y. Zhu, S. Yang, C. Cao, W. Song, L.-J. Wan, Controllable synthesis of carbon encapsulated iron phosphide nanoparticles for the chemoselective hydrogenation of aromatic nitroarenes to anilines, Inorg. Chem. Front. 5 (2018) 1094–1099.

[52] C. Zhao, X. Shao, Z. Zhu, C. Zhao, X. Qian, One-pot hydrothermal synthesis of RGO/FeS composite on Fe foil for high performance supercapacitors, Electrochim. Acta 246 (2017) 497–506.

[53] H. Wang, Y. Liang, Y. Li, H. Dai, Co $_{1-x}$ S – Graphene Hybrid: a high-performance metal chalcogenide electrocatalyst for oxygen reduction, Angew. Chem. Int. Ed. 50 (2011) 10969–10972.

[54] D. Jang, S. Lee, Y. Shin, S. Ohn, S. Park, D. Lim, G. Park, S. Park, $Ni-O_4$ species anchored on N-doped graphene-based materials as molecular entities and electrocatalytic performances for oxygen reduction reaction, Solid State Sci. 74 (2017) 56–61.

[55] Q. Dong, X. Zhuang, Z. Li, B. Li, B. Fang, C. Yang, H. Xie, F. Zhang, X. Feng, Efficient approach to iron/nitrogen co-doped graphene materials as efficient electrochemical catalysts for the oxygen reduction reaction, J. Mater. Chem. A 3 (2015) 7767–7772.

[56] M. Xiao, J. Zhu, L. Feng, C. Liu, W. Xing, Meso/macroporous nitrogen-doped carbon architectures with iron carbide encapsulated in graphitic layers as an efficient and robust catalyst for the oxygen reduction reaction in both acidic and alkaline solutions, Adv. Mater. 27 (2015) 2521–2527.

[57] L. Zhao, X.L. Sui, J.Z. Li, J.J. Zhang, L.M. Zhang, G.S. Huang, Z.B. Wang, Supramolecular assembly promoted synthesis of three-dimensional nitrogen doped graphene frameworks as an efficient electrocatalyst for oxygen reduction reaction and methanol electrooxidation, Appl. Catal. B Environ. 231 (2018) 224–233.